LPF-free Harmonic Current Control in Multi-synchronous Reference Frames for Dual Three-phase PMSMs

Yulei Yang, Qian Wang, *Member, IEEE*, Fangrui Wei, and Yichen Yu

***Abstract*—Harmonic current regulation in multi-phase motor drives remains challenging under dynamic operating conditions due to non-sinusoidal back electromotive force (EMF) and inverter nonlinearities, which introduce dominant low-order harmonics. Multi-synchronous reference frame (MSRF) based methods are widely adopted for multi-frequency current regulation; however, conventional implementations typically rely on low-pass filters (LPFs) for harmonic decoupling, introducing detection delay and phase distortion that limit transient performance. This paper proposes an LPF-free MSRF-based harmonic current control method for dual three-phase permanent magnet synchronous motor (DTP-PMSM) drives. By introducing harmonic transformation matrix coefficients (HTMCs), the proposed method retains the independent regulation of multiple harmonic components within the MSRF framework, while eliminating the filtering step in the harmonic decoupling path, without the need for harmonic plane reconstruction or additional coordinate transformations. To support adaptive changes, a Goertzel-based harmonic amplitude extraction scheme is employed to periodically update the HTMC. Experimental results demonstrate that the proposed method significantly enhances dynamic performance, achieving a 19.3% reduction in speed transition stabilization time compared to other methods. The proposed LPF-free formulation provides a practical solution for MSRF-based harmonic current control in industrial motor drive applications where fast dynamic response is required.**

***Index Terms*—Low-pass filter (LPF)-free harmonic decoupling, Multi-synchronous reference frame (MSRF), Multi-frequency current control, Harmonic current suppression, Industrial motor drives, Dual three-phase permanent magnet synchronous motors (DTP-PMSMs).**

Manuscript received December 28, 2025; revised March 03, 2026; accepted March 25, 2026. Date of publication June 25, 2026. Date of current version Aril 17, 2026.

This work was supported in part by the National Natural Science Foundation of China under Grant 52277039, in part by the Heilongjiang Province Postdoctoral Science Foundation under Grant LBH-Z23178, and in part by the National Key Laboratory of Robotics Technology and Systems under Grant SKLRS202407B.

Yulei Yang is with the Harbin Institute of Technology, Harbin, Heilongjiang 150001, China (e-mail: 21B906021@stu.hit.edu.cn).

Qian Wang and Fangrui Wei are with Harbin Institute of Technology, Harbin, Heilongjiang 150001, China (e-mail: q.wang@hit.edu.cn; weifangrui @hit.edu.cn).

Yichen Yu is with Electrical Engineering Department, Harbin Institute of Technology, Harbin, Heilongjiang 150001, China (e-mail: 22B906037@stu. hit.edu.cn).

(*Corresponding author: Qian Wang*)

Digital Object Identifier 10.30941/CESTEMS.2026.00013

I. INTRODUCTION

DUAL three-phase permanent magnet synchronous motors (DTP-PMSMs) are widely used in high-reliability and high-performance application areas such as aerospace, marine equipment, and rail transportation due to their advantages, such as low torque ripple, high redundancy, and strong fault tolerance [1]-[3]. Currently, the commonly used modeling method for DTP-PMSM is vector space decomposition (VSD) [4]-[6]. This method decouples the motor variables in the six-phase stationary coordinate system using a six-dimensional transformation matrix and maps them into three mutually independent subspaces: the fundamental frequency subspace, the harmonic subspace, and the zero-sequence subspace. Ideally, the current in the harmonic subspace should be zero. However, in practical systems, factors such as non-sinusoidal back electromotive force (EMF), dead zone effects, and non-sinusoidal waveform drive result in harmonic currents in the DTP-PMSM [6]-[7]. These harmonic currents are primarily composed of the 5th and 7th harmonics [8]-[9]. On one hand, current harmonics generate losses, affecting system efficiency. On the other hand, if the current reference is set to a pre-designed non-sinusoidal waveform, harmonic currents can be injected to increase average torque [10]-[11] or minimize torque ripple [12]. However, whether suppressing or injecting harmonics, a current harmonic control system with good steady-state and dynamic performance is required.

There are many existing methods developed for harmonic current regulation. For the VSD model of the DTP-PMSM, [13]-[14] proposed a combined method using a proportional-integral (PI) controller and a multi-resonant controller to suppress the 5th and 7th harmonic currents caused by system nonlinearities. Reference [15] combines adaptive linear neurons (ALN) with PI controllers to achieve better harmonic current suppression. In [16]-[17], extended state observers (ESO) and generalized integrators (GIs) are also applied for harmonic current suppression. However, these methods exhibit limited tracking capability for harmonic current references, rendering them unsuitable for harmonic current injection scenarios [18]. Furthermore, model predictive control (MPC) [19]-[21], direct torque control (DTC) [22]-[23], and optimized modulation strategies [24]-[25] are also widely used in harmonic current suppression. These methods

perform well in current regulation but may suffer from high torque ripple or computational burdens [18].

The multi-synchronous reference frame (MSRF), which treats the motor system as multiple subsystems of different harmonic orders within MSRFs and achieves fundamental and harmonic current control through independent decoupling of the required current loops [26]-[27], is also a commonly adopted method. In DTP-PMSM systems, [18] generates auxiliary currents by applying phase shifts of π/9 and π/18 to the physical currents, and subsequently employs complex vector PI controllers for harmonic current regulation. However, this method requires the use of low-pass filters (LPFs) for harmonic suppression, which introduces significant time delays, degrades the current dynamic response, and undermines the stability of the control system [18]. References [28]-[29] achieve complete decoupling of different harmonic current orders by reconstructing the harmonic subspace, without requiring LPFs. In [28], a virtual multi-three-phase system is constructed, utilizing a higher-dimensional VSD to map different harmonic components into isolated subspaces. Although this method achieves filter-free decoupling, it relies on multi-angle phase-shifting operations of the physical phase currents. The accuracy of the phase shifting is significantly affected by discrete sampling errors. Even with linear interpolation compensation, such errors can only be reduced, not completely eliminated. In [29], harmonic subspace reconstruction is performed in the rotating reference frame, leveraging the rotational speed characteristics of the 5th and 7th harmonic vectors to achieve natural decoupling. However, this method remains susceptible to phase errors induced by discrete sampling in practical implementations. Moreover, the reconstruction process introduces additional algorithmic complexity, imposing higher demands on the real-time computational capability of the controller.

To this end, this paper proposes and experimentally validates an innovative LPF-free MSRF-based harmonic current control method for DTP-PMSMs, where harmonic transformation matrix coefficients (HTMCs) eliminate the need for traditional filtering stages, enabling independent regulation of multiple harmonic components without the need for harmonic plane reconstruction or additional coordinate transformations. Additionally, a Goertzel-based harmonic amplitude extraction scheme supports periodic updates of the HTMCs, enhancing the system's real-time performance. The innovations of the paper are as follows:

1) The HTMC is proposed and integrated into the MSRF method, eliminating the need for LPFs.

2) A Goertzel-based method is employed to extract harmonic current amplitudes from complex signals, ensuring the periodic updating of the HTMC and enabling the proposed method to achieve adaptiveness.

3) Compared to existing MSRF methods, the proposed approach eliminates the need to reconstruct the harmonic current plane, perform phase shifts, or apply shaft rotations, demonstrating more stable harmonic suppression and stronger dynamic performance during motor dynamic processes.

The structure of this paper is as follows. Section II introduces the current harmonic analysis of DTP-PMSM. Section III analyzes the proposed method. Section IV provides experimental results and discussion. Finally, Section V presents the conclusions of this paper.

II. Current Harmonic Analysis of DTP-PMSM

The DTP-PMSM is comprised of two sets of Y-connected windings, ABC and DEF, with a 30° electrical offset. The structure of its control system is illustrated in Fig. 1. Utilizing the VSD approach, the physical quantities in the natural coordinate system of the DTP-PMSM can be transformed into three orthogonal, decoupled subspaces: the α-β, z_1-z_2, and o_1-o_2 subspace. This paper utilizes a DTP-PMSM with neutral point isolation, where no current flows in the o_1-o_2 subspace, allowing it to be neglected. The transformation matrices for the remaining two subspaces are presented:

$$\begin{bmatrix} F_\alpha & F_\beta & F_{z1} & F_{z2} \end{bmatrix}^{\mathrm{T}} = \boldsymbol{T}_{6s/2s} \begin{bmatrix} F_A & F_B & F_C & F_D & F_E & F_F \end{bmatrix}^{\mathrm{T}} \quad (1)$$

where F_α, F_β, F_{z1}, and F_{z2} represent the voltages, currents, or flux along the α-axis, β-axis, z_1-axis, and z_2-axis, respectively. $\boldsymbol{T}_{6s/2s}$ denotes the VSD transformation matrix. The variables F_A, F_B, F_C, F_D, F_E, and F_F correspond to the six-phase voltages, currents, or flux of the DTP-PMSM.

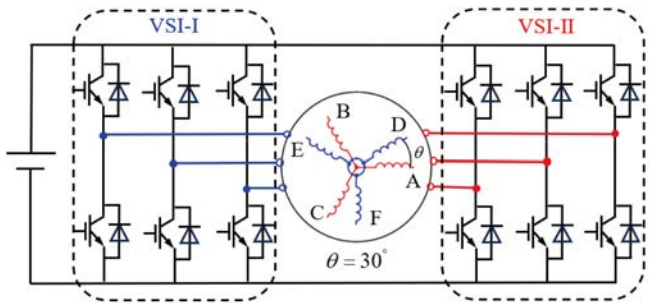

Fig. 1. DTP-PMSM system.

A. Non-sinusoidal Back EMF

Typically, due to factors such as mechanical design, electromagnetic design, and manufacturing errors, harmonic components are present in the motor's back EMF. Completely eliminating these harmonics is extremely challenging in practical applications. Fig. 2 presents the back EMF and its spectral distribution for the motor used in this experiment, where the 5th and 7th harmonic components are particularly prominent. In practical applications, these harmonic currents not only affect the torque characteristics of the motor, causing torque ripple, but also contribute to increased power losses.

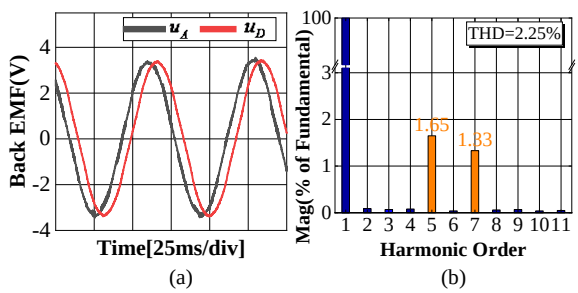

(a) (b)

Fig. 2. Back EMF and FFT analysis. (a) Back EMF. (b) FFT.

B. *Inverter Nonlinearity*

Inverter nonlinearity arises from several factors, including the dead-time effect and the voltage drop across the insulated-gate bipolar transistor (IGBT) switches. Among these, the impact of the dead-time effect is particularly significant. Taking phase A as an example, the voltage error due to the dead-time effect within a single pulse width modulation (PWM) cycle can be represented as [30]:

$$\Delta u_{\mathrm{A}} = \Delta u_{\mathrm{e}} \cdot \mathrm{sign}\left(i_{\mathrm{A}}\right), \quad \mathrm{sign}\left(i_{\mathrm{A}}\right) = \begin{cases} 1, & i_{\mathrm{A}} > 0 \\ -1, & i_{\mathrm{A}} < 0 \end{cases} \tag{2}$$

where sign() denotes the sign function, Δu_{e} represents the voltage error and i_{A} represents the A-phase current.

The six-phase voltage error, when transformed into the stationary coordinate system using VSD, can be expressed as:

$$\begin{cases} \Delta u_{\alpha\_\mathrm{N}} = \dfrac{4}{\pi}\Delta u_{\mathrm{e}}\left(\dfrac{1}{11}\sin 11\omega_{\mathrm{e}}t + \dfrac{1}{13}\sin 13\omega_{\mathrm{e}}t\right) \\ \Delta u_{\beta\_\mathrm{N}} = -\dfrac{4}{\pi}\Delta u_{\mathrm{e}}\left(-\dfrac{1}{11}\cos 11\omega_{\mathrm{e}}t + \dfrac{1}{13}\cos 13\omega_{\mathrm{e}}t\right) \\ \Delta u_{z1\_\mathrm{N}} = \dfrac{4}{\pi}\Delta u_{\mathrm{e}}\left(\dfrac{1}{5}\sin 5\omega_{\mathrm{e}}t + \dfrac{1}{7}\sin 7\omega_{\mathrm{e}}t\right) \\ \Delta u_{z2\_\mathrm{N}} = -\dfrac{4}{\pi}\Delta u_{\mathrm{e}}\left(\dfrac{1}{5}\cos 5\omega_{\mathrm{e}}t - \dfrac{1}{7}\cos 7\omega_{\mathrm{e}}t\right) \end{cases} \tag{3}$$

where ω_{e} represents the fundamental angular frequency.

As shown in (3), after the phase voltage error of the DTP-PMSM is transformed using $\boldsymbol{T}_{6\mathrm{s}/2\mathrm{s}}$, the α-β subspace contains the fundamental and 12k±1 (where k is a natural number) harmonic components, whereas the z_1-z_2 subspace contains 6k±1 harmonic components. The current in the z_1-z_2 subspace is entirely converted into harmonic losses.

Based on the above analysis, it can be concluded that the harmonic current in the z_1-z_2 subspace is primarily composed of the 5th and 7th harmonics, with possible contributions from the 11th and 13th harmonics. This paper focuses on the primary harmonics as the research object, and the harmonic subspace current components can be approximated as (4):

$$\begin{cases} i_{z1} = A_5\cos\left(5\omega_{\mathrm{e}}t + \phi_5\right) + A_7\cos\left(7\omega_{\mathrm{e}}t + \phi_7\right) \\ i_{z2} = A_5\sin\left(5\omega_{\mathrm{e}}t + \phi_5\right) + A_7\sin\left(7\omega_{\mathrm{e}}t + \phi_7\right) \end{cases} \tag{4}$$

where A_i and ϕ_i (i = 5, 7) denote the amplitude and phase of the harmonic currents, respectively.

III. Proposed LPF-free MSRF Strategy for Harmonic Current Suppression

A. *Proposed LPF-free MSRF Method based on HTMC*

From the VSD transformation matrix and the dual α-β transformation procedure ($\boldsymbol{T}_{6\mathrm{s}/2\alpha\beta}$ is provided in the Appendix), the following relationship can be obtained:

$$\begin{bmatrix} i_{\alpha} \\ i_{\beta} \\ i_{z1} \\ i_{z2} \end{bmatrix} = \frac{1}{2}\begin{bmatrix} 1 & 0 & 1 & 0 \\ 0 & 1 & 0 & 1 \\ 1 & 0 & -1 & 0 \\ 0 & -1 & 0 & 1 \end{bmatrix}\begin{bmatrix} i_{\alpha1} \\ i_{\beta1} \\ i_{\alpha2} \\ i_{\beta2} \end{bmatrix} \tag{5}$$

where $i_{\alpha1}$ and $i_{\beta1}$ denote the a-axis and β-axis currents of the first winding set, while $i_{\alpha2}$ and $i_{\beta2}$ represent the α-axis and β-axis currents of the second winding set.

Fig. 3 illustrates the vector diagram corresponding to the relationship described in (5). According to Fig. 3, when the synchronous frame rotates counterclockwise, the harmonic subspace frame spans from z_2 to z_1, corresponding to a clockwise orientation. In addition, the 5th and 7th harmonics resulting from nonlinear effects such as dead-time are also located in the harmonic subspace. Their transformation into the proposed synchronous reference frames is illustrated in Fig. 4.

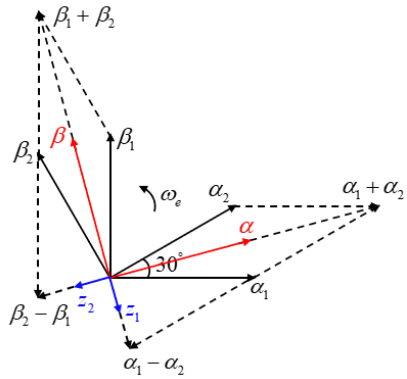

Fig. 3. Vector relations of the two transformation methods.

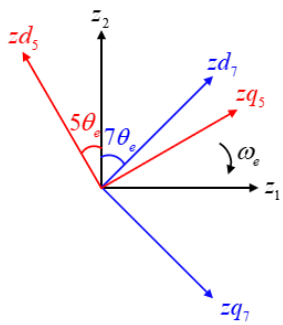

Fig. 4. Diagram of the proposed MSRFs for the harmonic subspace.

The proposed MSRF is based on the z_2-axis and adopts a clockwise-rotating synchronous frame. In other words, the electrical angle in the transformation process is defined as the angle between the zd-axis of the synchronous frame and the z_2-axis. The detailed harmonic transformation process is as follows:

$$\begin{bmatrix} i_{\mathrm{zd5}} \\ i_{\mathrm{zq5}} \end{bmatrix} = k_5\begin{bmatrix} -\sin 5\theta_{\mathrm{e}} & \cos 5\theta_{\mathrm{e}} \\ \cos 5\theta_{\mathrm{e}} & \sin 5\theta_{\mathrm{e}} \end{bmatrix}\begin{bmatrix} i_{z1} \\ i_{z2} \end{bmatrix} \tag{6}$$

$$\begin{bmatrix} i_{\mathrm{zd7}} \\ i_{\mathrm{zq7}} \end{bmatrix} = k_7\begin{bmatrix} \sin 7\theta_{\mathrm{e}} & \cos 7\theta_{\mathrm{e}} \\ \cos 7\theta_{\mathrm{e}} & -\sin 7\theta_{\mathrm{e}} \end{bmatrix}\begin{bmatrix} i_{z1} \\ i_{z2} \end{bmatrix} \tag{7}$$

where k_5 and k_7 are the HTMC, which are determined based on the amplitude of the corresponding harmonic currents.

The proposed HTMC in this paper is intended to replace the LPF in conventional MSRF methods. The LPF filters out the high-frequency harmonics after coordinate transformation while retaining the desired direct current (DC) currents. In

contrast, the proposed HTMC is designed to attenuate the amplitudes of high-frequency harmonics. After the same harmonic currents i_{z1} and i_{z2} undergo two consecutive coordinate transformations, the 5th and 7th harmonic currents are converted into DC components, whereas harmonic currents at other frequencies persist and their amplitudes remain unchanged. When the post-control 5th and 7th harmonic currents are summed to obtain the required reference voltage, these other harmonic components also accumulate, potentially causing the amplitude of the uncontrolled harmonics to exceed their original range. In addition, the input signal to the inverter must satisfy the normalization requirement. The role of the HTMC is thus to maintain the amplitudes of these uncontrolled harmonic currents within their original limits. Therefore, HTMC is defined as the proportion of the amplitudes of the controlled harmonic currents at different frequencies, and the condition for system stability is that $k_5 + k_7 \le 1$.

Assuming the amplitudes of the 5th and 7th harmonics are A_5 and A_7, respectively, the HTMC can be expressed as:

$$k_i = \frac{A_i}{A_5 + A_7} \tag{8}$$

Therefore, by applying transformations (6) and (7), the corresponding 5th harmonic current and 7th harmonic current can be effectively extracted within the harmonic subspace. The following section presents how the harmonic amplitudes used to define the HTMC are obtained.

B. Calculation of HTMC based on the Goertzel Algorithm

The Goertzel algorithm is an efficient method for computing the discrete Fourier transform (DFT) at specific frequencies of interest. Unlike the full DFT, it selectively calculates only the required frequency components, thereby significantly reducing computational complexity. In this paper, the algorithm is adapted and applied to extract harmonic current amplitudes in real time, with its structure tailored to meet the timing and accuracy constraints of resource-constrained embedded motor control systems. Fig. 5 illustrates the implementation of the proposed approach based on the Goertzel structure.

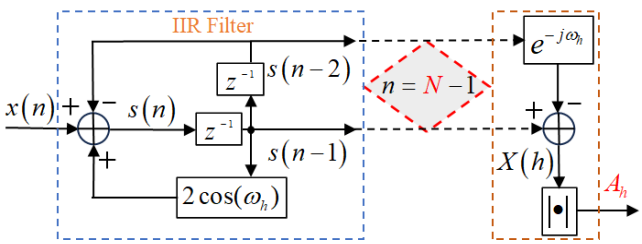

Fig. 5. Block diagram of harmonic amplitude computation based on the Goertzel algorithm.

Assume the discrete signal is $x(n)$, where n = 0, 1, 2, …, N−1. Our objective is to compute the DFT coefficient $X(h)$ corresponding to a specific frequency ω_h of the discrete signal $x(n)$. The standard definition of the DFT is:

$$X(h) = \sum_{n=0}^{N-1} x(n) \cdot e^{-j\omega_h} \tag{9}$$

where h represents the order of the harmonic component, and N denotes the sampling window length.

For a discrete signal with a fundamental frequency f_1 and a sampling rate $f_s = 1/T_s$, where T_s is the sampling period, the angular frequency of the h^{th} harmonic based on the sampling rate is given by:

$$\omega_h = \frac{2\pi h f_1}{f_s} \tag{10}$$

Subsequently, an infinite impulse response (IIR) filter with a designated resonant frequency is applied to perform harmonic signal extraction through a recursive computation. The system function of the corresponding filter is formulated as (11):

$$H(z) = \frac{1 - e^{-j\omega_h z^{-1}}}{1 - 2\cos(\omega_h) z^{-1} + z^{-2}} \tag{11}$$

As shown in (11), this filter is a band-pass filter centered at ω_h. Since the denominator is a second-order polynomial, it is classified as a second-order IIR filter. The poles lie on the unit circle at $z = e^{\pm j\omega_h}$, indicating that the filter exhibits a strong response at ω_h. The output of the filter represents the accumulated response of the ω_h component in the input signal. By introducing a state variable, the difference equation corresponding to (11) can be expressed as:

$$s(n) = 2\cos(\omega_h) s(n-1) - s(n-2) + x(n) \tag{12}$$

where $s(n)$ is the internal state variable of the filter.

Finally, at $n = N - 1$, the complex spectral value corresponding to the target frequency is given by:

$$X(h) = s(N-1) - e^{-j\omega_h} s(N-2) \tag{13}$$

By applying Euler's formula to expand the complex spectrum, the real and imaginary parts are obtained as:

$$\begin{cases} \mathrm{Re}[X(k)] = s(N-1) - \cos(\omega_h) s(N-1) \\ \mathrm{Im}[X(k)] = \sin(\omega_h) s(N-2) \end{cases} \tag{14}$$

Then, the amplitude of the harmonic component at angular frequency ω_h can be expressed as:

$$\begin{aligned} A_h &= \sqrt{[s(N-1) - \cos(\omega_h) s(N-2)]^2 + [\sin(\omega_h) s(N-2)]^2} \\ &= \sqrt{s(N-1)^2 + s(N-2)^2 - 2\cos(\omega_h) s(N-1) s(N-2)} \end{aligned} \tag{15}$$

By applying the Goertzel algorithm to two selected target frequencies, the amplitudes corresponding to the desired harmonic components can be obtained with relatively low computational cost.

C. Design Principle for the Sampling Window Length N

In the process of harmonic amplitude extraction, the sampling window length N has a significant impact on the accuracy of amplitude computation. Ideally, N should be chosen such that the target frequency f_t aligns exactly with a DFT frequency bin m, satisfying the condition:

$$m = \frac{N f_t}{f_s} \in Z \tag{16}$$

where Z is an integer.

However, the ideal conditions mentioned above apply to extracting the amplitude of a single frequency, whereas this paper requires simultaneously solving for the harmonic current amplitudes at two frequencies. Under transient conditions, it may be impossible to find a suitable value of N that ensures perfect alignment for all target frequencies. The reason is that when N satisfies precise alignment for both frequencies simultaneously, it will result in a very large N value. First, this would introduce a significant delay; second, a larger N would consume more computational resources. Therefore, to balance these two factors, the selected N does not precisely align both frequencies, resulting in alignment errors. Such misalignment can lead to spectral leakage, which in turn causes amplitude estimation errors. The following content will discuss the impact of the sampling window length N on the accuracy of amplitude extraction under frequency alignment errors.

Suppose a composite input signal is given as follows:

$$x = 5\sin\left(2\pi f_t t\right) + 1.5\sin\left(10\pi f_t t + 4\pi/3\right) + 0.5\cos\left(20\pi f_t t\right) \quad (17)$$

where t represents discrete time with an interval of T_s = 0.0001 s, which corresponds to the period of the PWM signal. The sampling rate is f_s = 10 kHz.

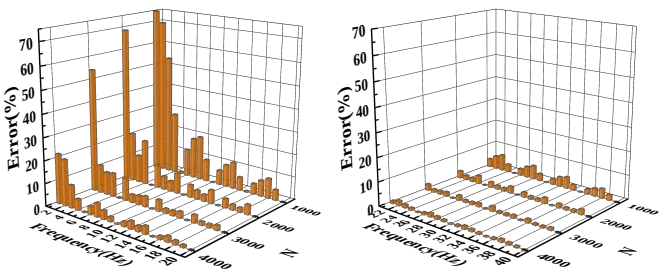

(a) (b)

Fig. 6. Error in harmonic amplitude extraction from complex input signals based on the Goertzel algorithm for different values of N. (a) The frequency is no greater than 20 Hz. (b) The frequency is greater than 20 Hz and no greater than 40 Hz.

Fig. 6 shows the error results of harmonic amplitude extraction using the Goertzel algorithm for complex input signals. As observed from Fig. 6, the value of N affects the harmonic amplitude extraction error, with larger values of N resulting in smaller errors. However, in practical applications, a larger N leads to a greater computational load, occupying more microcontroller unit (MCU) resources. Therefore, the selection of N should be based on the computational capacity of the actual system. Additionally, the results in Fig. 6 demonstrate that the harmonic amplitude extraction error is related to the fundamental frequency f_1. Fig. 6(a) indicates that when the fundamental frequency f_1 is no greater than 20 Hz, the extracted harmonic amplitude error is significant, and even increasing the value of N does not yield an acceptable reduction in error. On the other hand, Fig. 6(b) shows that when f_1 exceeds 20 Hz, the impact of N on harmonic extraction error diminishes significantly. In this case, when N exceeds 2000, the amplitude extraction error remains almost constant.

To address the issue of large errors at low frequencies, a segmented approach is adopted for determining the harmonic matrix coefficients. When the fundamental frequency f_1 is below 20 Hz, fixed coefficients are used. Specifically, the amplitude proportions of the 5th and 7th harmonics are analyzed at f_1 = 5 Hz and f_1 = 15 Hz to determine appropriate values for the coefficients. In this study, the selected coefficients are k_5 = 0.5 and k_7 = 0.5. For f_1 above 20 Hz, the harmonic matrix coefficients are determined based on the amplitudes extracted using the Goertzel algorithm. According to Fig. 6(b), the value of N is set to 2000, which ensures both the accuracy of amplitude extraction and the real-time performance of the system.

Fig. 7 presents the flowchart of the HTMC update procedure. As illustrated in Fig. 7, the initial values are set to k_5 = 0.5 and k_7 = 0.5. When the fundamental frequency $f_1 \le 20$ Hz, the HTMC is not updated and retains its initial values. When f_1 > 20 Hz, the HTMC calculation based on the Goertzel algorithm is activated. Upon the completion of N = 2000 sampling points, the HTMC coefficients are updated. If the computation for N = 2000 has not yet been completed, the HTMC coefficients remain unchanged.

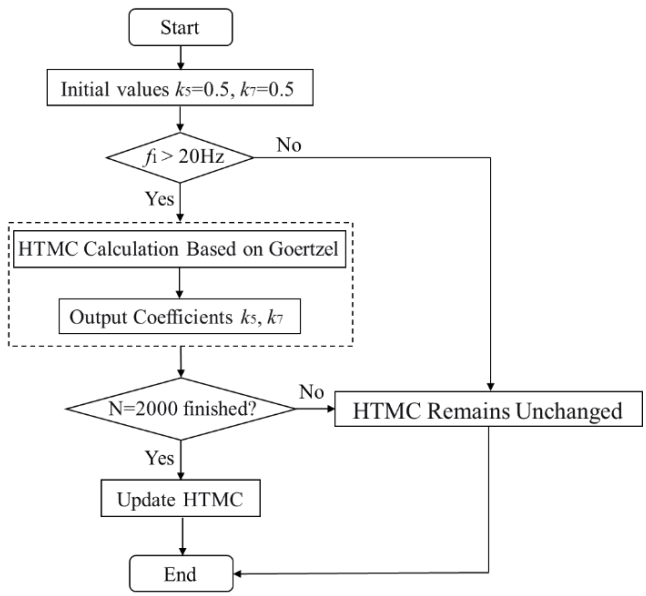

Fig. 7. Flowchart of the HTMC update process.

D. Harmonic Suppression Control Strategy

Fig. 8 illustrates the control system block diagram for harmonic current suppression in a DTP-PMSM using the proposed MSRF method. The speed loop and the dq-axis current loops both adopt PI control strategies. Harmonic currents in the harmonic subspace are obtained via the VSD decoupling method and are processed using the proposed MSRF approach to extract the 5th and 7th harmonic currents. This transformation converts periodic sinusoidal harmonic currents into DC signals in a rotating reference frame, enabling effective suppression or even elimination of the 5th and 7th harmonic currents through PI controllers. The Goertzel algorithm is employed to scale the transformed harmonic currents to appropriate amplitudes, ensuring that the inverter input satisfies normalization requirements.

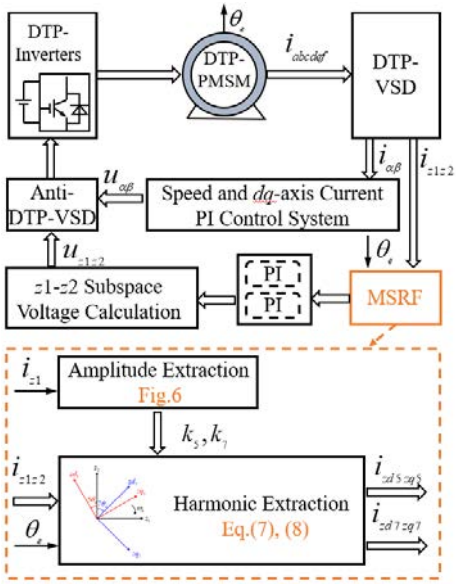

Fig. 8. Block diagram of the harmonic suppression control system for DT-PMSM.

IV. Experimental Verification and Discussion

The experimental platform for the DTP-PMSM is shown in Fig. 9. The neutral points of the DTP-PMSM are left unconnected, and its parameters are listed in Table I. The main control unit of the controller is the DSP28379D. The PWM switching frequency is set to 10 kHz with a dead time of 3 μs. An eddy current brake is employed as the load.

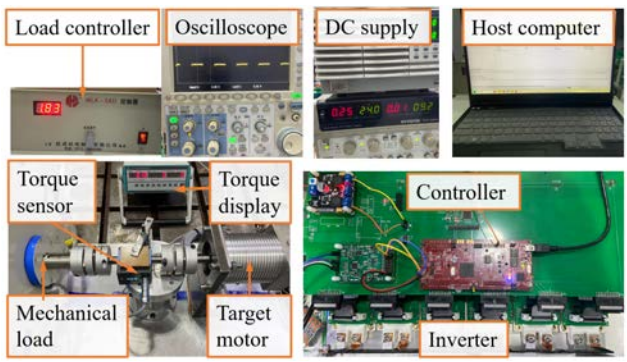

Fig. 9. Experimental platform.

TABLE I
DT-PMSM PARAMETERS

Parameters	Values	Parameters	Values
Rated power, P_r /kw	1	Number of poles/slots	10/12
Bus voltage, V_{dc} /V	50	Phase resistance, R_s /Ω	0.11
Rated current, I_r /A	3.5	Synchronous inductor, L_{dq} /(mH)	2.55
Rated torque, T_r /(N·m)	5	Leakage inductance, L_z /(mH)	0.8
Rated speed, n_r /(r·min^{-1})	800	Permanent magnet flux, φ_f /Wb	0.237

A. Experimental Validation

To verify the existence of coupling effects between different harmonic suppression loops, a selective harmonic current suppression experiment is conducted under rated speed and load conditions, as shown in Fig. 10. In Period 1, both the 5th and 7th harmonic currents are suppressed, causing the phase currents (i_A and i_D) to approximate sinusoidal waveforms, while the harmonic currents i_{z1} and i_{z2} become almost negligible. In Period 2, the 7th harmonic current is not suppressed, but the 5th harmonic current is, resulting in fluctuations in the harmonic currents and a slight increase in i_{z1} and i_{z2}. In Period 3, neither the 5th nor the 7th harmonic currents are suppressed, leading to significant fluctuations in the harmonic currents, a notable increase in i_{z1} and i_{z2}, and increased phase current distortion. Specifically, the harmonic current content reaches its highest level, with a clear combination of the 5th and 7th harmonics. These results demonstrate that suppressing one harmonic does not significantly affect the other, indicating effective decoupling between the multi-frequency harmonic control loops.

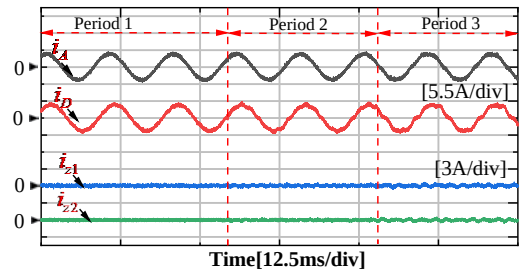

Fig. 10. Current response under selective harmonic current suppression.

To investigate the influence of different HTMC combinations on system performance, experiments were conducted by varying the HTMC values for the 5th and 7th harmonic currents. Table II presents the experimental results for HTMC combinations with k_5 and k_7 set to 0.2, 0.4, 0.6, and 0.8, respectively. Under rated speed and operating conditions, the HTMC values determined based on the amplitudes of the 5th and 7th harmonic currents are 0.72 and 0.28, respectively. The range of HTMC combinations designed for the experiments covers the actual values under rated operating conditions. The results in Table II indicate that when $k_5 + k_7 \leq 1$, the motor operates normally. Conversely, when this condition is violated, the experimental process triggers a protection mechanism, preventing the motor from operating properly. Furthermore, the various HTMC combinations tested demonstrate that the proposed method allows for a certain margin of error in the coefficient settings. It is only when the deviation becomes sufficiently large, for instance, when the actual value of k_5 is 0.72 but is set to 0.2 in the experiment, that the system performance is noticeably affected.

To investigate the influence of the number of sampling points N on amplitude extraction error, code execution time, random access memory (RAM) utilization, and speed transition stabilization time, experiments were conducted under rated load conditions. Fig. 11 presents the experimental results for amplitude extraction error, code execution time, and RAM utilization when N is set to 1000, 2000, and 3000. The stabilization time during a step change in speed from 400 to 800 rad/min is also presented in Fig. 11. As illustrated in Fig. 11, the maximum amplitude extraction error is 13.7% when N = 1000, and the minimum error is 3.2% when N =

3000. Notably, the value of N has no appreciable impact on code execution time. This is because the HTMCs are calculated based on a sliding window, with only one sampling point selected per computation cycle. The primary influence of N is on the memory utilization of the DSP28379D, a larger N results in higher memory consumption. When N is set to 1000, 2000, and 3000, the corresponding RAM utilization ratios are 32.6%, 43.1%, and 54.8%, respectively. Furthermore, N determines the update delay of the HTMCs. Theoretically, given a switching frequency of 10 kHz, the delay is 0.1 s for N = 1000 and 0.3 s for N = 3000. During speed transient conditions, the stabilization time with N = 1000 is only 0.02 s longer than that with N = 2000 or N = 3000, indicating a relatively minor effect. The comprehensive experimental results suggest that N should not be set too large, as this increases memory usage and delay, nor too small, as this leads to significant amplitude extraction error. Accordingly, N = 2000 represents a reasonable trade-off that balances accuracy, memory efficiency, and dynamic performance.

TABLE II
EXPERIMENTAL RESULTS FOR DIFFERENT HTMC COMBINATIONS

k_5	k_7	k_5 + k_7	Operation	THD of i_A/%	Harmonic current/A	
					5th	7th
0.2	0.2	0.4	√	8.25	0.21	0.07
	0.4	0.6	√	8.26	0.22	0.05
	0.6	0.8	√	8.17	0.18	0.05
	0.8	1	√	8.21	0.20	0.05
0.4	0.2	0.6	√	7.65	0.06	0.06
	0.4	0.8	√	7.61	0.04	0.04
	0.6	1	√	7.63	0.06	0.06
	0.8	1.2	×	—	—	—
0.6	0.2	0.8	√	7.62	0.05	0.04
	0.4	1	√	7.63	0.04	0.06
	0.6	1.2	×	—	—	—
	0.8	1.4	×	—	—	—
0.8	0.2	1	√	7.65	0.05	0.05
	0.4	1.2	×	—	—	—
	0.6	1.4	×	—	—	—
	0.8	1.6	×	—	—	—

B. *Steady-state Comparison with Other Methods*

The experiment shown in Fig. 10 verifies that the proposed method effectively suppresses the harmonic currents of the DTP-PMSM, decouples and suppresses each harmonic current independently, and ensures that they do not interfere with each other. To highlight the contribution of this paper, a steady-state experimental comparison is conducted between the proposed method and other existing methods. Fig. 12 compares the current waveforms and fast Fourier transform (FFT) results for four different methods at rated load and a speed of 800 r/min. Method 1 uses a traditional PI controller, Method 2 employs the MSRF-based virtual multi three-phase systems (VMTPS) method described in [28], and Method 3 utilizes the MSRF-RCS-based method presented in [29]. Following the PI parameter tuning logic in [28]-[29], the parameters were determined using the zero-pole cancellation method, where $K_p = K_{ch} \times L$ and $K_i = K_{ch} \times R$. Let K_p and K_i denote the proportional and integral gains of the PI controller, respectively. K_{ch} represents the bandwidth of the current loop. For the fundamental frequency current loop, L represents the synchronous inductance and R is the phase resistance. For the harmonic current loop, the 5th and 7th harmonic currents share the same parameters, with L denoting the leakage inductance and R the phase resistance. Therefore, the comparative method and the proposed method adopt the same current-loop parameters. In addition, all methods share identical speed-loop parameters. The detailed parameters are provided in Table III. According to the parameter tuning rule for the second-order LPF in [28], the damping ratio is selected as 0.707, and the cutoff frequency of the LPF in the fundamental current loop is set higher than that in the 5th and 7th harmonic current loops. Therefore, following the parameter selection in [28], the cutoff frequency of the LPF for the fundamental current loop is set to 377 rad/s, while the cutoff frequency of the LPFs for the 5th and 7th harmonic current loops is set to 125.66 rad/s.

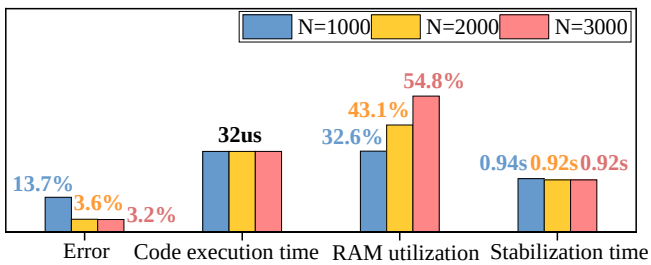

Fig. 11. Experimental results of amplitude extraction error, code execution time, RAM utilization, and speed transition stabilization time for different values of N.

TABLE III
CONFIGURATION OF CORE CONTROLLER PARAMETERS

Cascade control structure	Method	K_p	K_i
Fundamental current loop	Method 1	3.36	145.14
	Method 2	3.36	145.14
	Method 3	3.36	145.14
	Proposed method	3.36	145.14
Harmonic current loop	Method 1	1.06	145.14
	Method 2	1.06	145.14
	Method 3	1.06	145.14
	Proposed method	1.06	145.14
Speed loop	Method 1	0.018	0.58
	Method 2	0.018	0.58
	Method 3	0.018	0.58
	Proposed method	0.018	0.58

Fig. 12(a) shows that the A-phase and D-phase current distortion is significant when using Method 1, with total harmonic distortion (THD) rates of 31.74% and 31.69%, respectively. The harmonic current waveforms exhibit noticeable low-frequency ripples, primarily dominated by the

5th and 7th harmonics, indicating that the traditional PI method is insufficient for suppressing harmonic currents in DTP-PMSM. In contrast, Figs. 12(b)-12(d) demonstrate that Methods 2, 3, and the proposed method effectively suppress harmonic currents in DTP-PMSM, with the phase currents exhibiting smooth sinusoidal waveforms. The phase current THDs for the three methods are similar, and the 5th and 7th harmonics are also effectively suppressed.

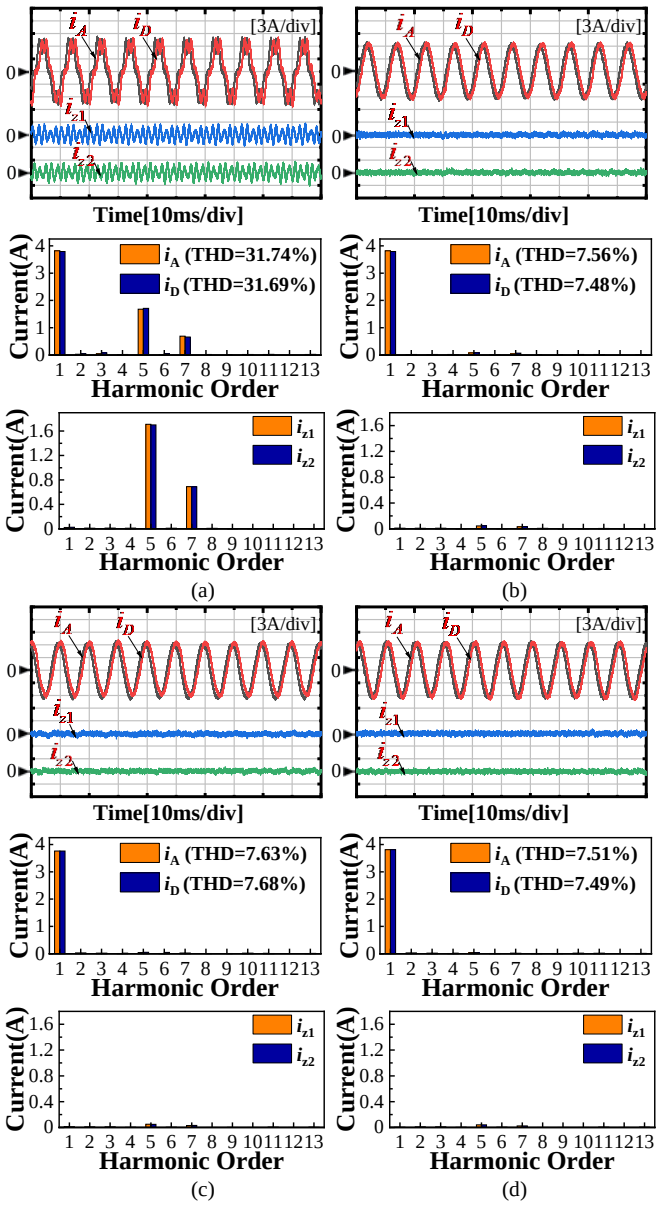

Fig. 12. Current and FFT results under rated load conditions at a speed of 800 r/min. (a) Method 1. (b) Method 2. (c) Method 3. (d) Proposed method.

Table IV compares the experimental results of the five methods at different speeds (20, 400, and 800 r/min) under rated load. The results include the root mean square (RMS) values of the phase A and phase D currents, the THD of both phases, and the amplitudes of the 5th and 7th harmonic currents. The table shows that for all methods, the THD of the phase A and phase D currents remains similar across different speeds, indicating the symmetry of the DTP-PMSM system structure. Method 1 shows high harmonic distortion for both phase A and phase D at all speeds. Although the THD improves slightly at higher speeds, it remains significant. At 20 r/min, the THD of phase A is 32.31%; at 400 r/min, the THD of phase A is 31.99%; and at 800 r/min, the THD of phase A is 31.74%. Methods 2, 3, and the proposed method show better harmonic suppression than Method 1 across all speed ranges. Compared to Method 1, the other three methods significantly reduce the 5th and 7th harmonic currents. The proposed method achieves THDs of 8.15%, 7.61%, and 7.51% for phase A current at different rotational speeds, respectively. These results show that, under steady-state conditions, the proposed method performs comparably to Methods 2 and 3 in terms of harmonic current suppression. It effectively reduces harmonic distortion in DTP-PMSMs and exhibits stable harmonic current suppression performance.

TABLE IV
COMPARISON OF EXPERIMENTAL RESULTS OF FOUR METHODS AT DIFFERENT SPEEDS

Method	Speed /(r·min^{-1})	i_A/A	i_D/A	THD of i_A/%	THD of i_D/%	Harmonic current/A	
						5th	7th
Method 1	20	3.87	3.89	32.31	32.28	1.65	0.63
	400	3.86	3.88	31.99	32.05	1.56	0.59
	800	3.88	3.89	31.74	31.69	1.68	0.64
Method 2	20	3.72	3.75	8.21	8.19	0.05	0.03
	400	3.77	3.76	7.45	7.39	0.05	0.06
	800	3.86	3.85	7.56	7.48	0.06	0.04
Method 3	20	3.71	3.68	8.12	8.18	0.05	0.04
	400	3.78	3.76	7.51	7.49	0.06	0.07
	800	3.81	3.78	7.63	7.68	0.05	0.06
Proposed method	20	3.73	3.75	8.15	8.21	0.06	0.04
	400	3.82	3.81	7.61	7.58	0.03	0.05
	800	3.79	3.80	7.51	7.49	0.04	0.04

C. *Experiment under Dynamic Operation*

Since Method 1 lacks significant harmonic suppression capabilities, dynamic comparisons with other methods are not meaningful. Therefore, only Methods 2, 3, and the proposed method are compared dynamically. The results of speed-changing experiments under half-load conditions are shown in Fig. 13. For Method 2, when the speed changes, the q-axis current i_q experiences a transient overshoot at the switching instant but quickly stabilizes. Currents i_{z1} and i_{z2} remain relatively stable, though slight fluctuations are still observed during the speed transition. A zoomed-in image shows that it takes 1.2 s to reach stability when the speed changes from 400 to 800 r/min. For Method 3, currents i_{z1} and i_{z2} exhibit significant fluctuations during the speed change, with smaller amplitudes than those of Method 2. The zoomed-in image shows that it takes 1.14 s to stabilize when the speed changes from 400 to 800 r/min. In contrast, the proposed method maintains system stability throughout the speed transition, with virtually no fluctuations. The zoomed-in image shows that it takes only 0.92 s to reach stability when the speed changes from 400 to 800 r/min. These results demonstrate that the proposed method maintains stable harmonic current suppression during speed variation and achieves a faster dynamic response.

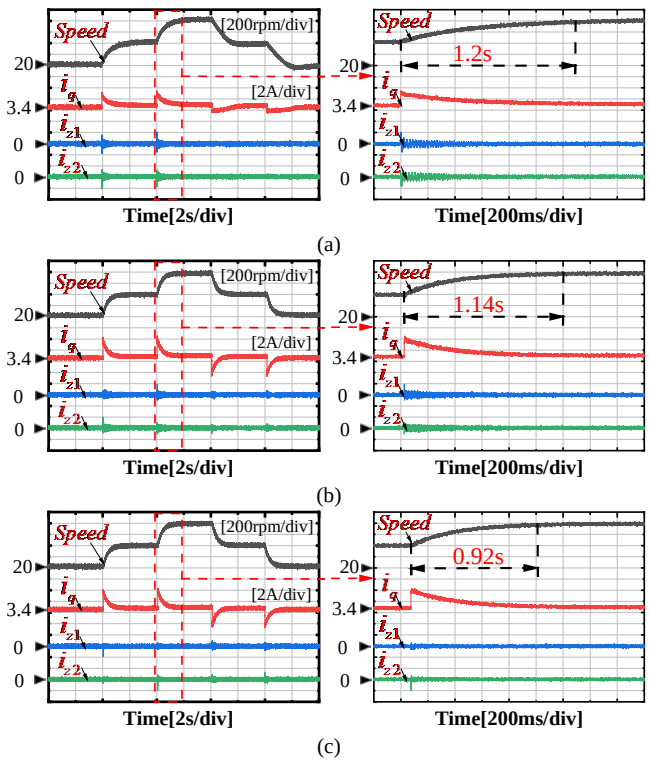

Fig. 13. Comparative experimental results of four different methods with speed variation. (a) Method 2. (b) Method 3. (c) Proposed method.

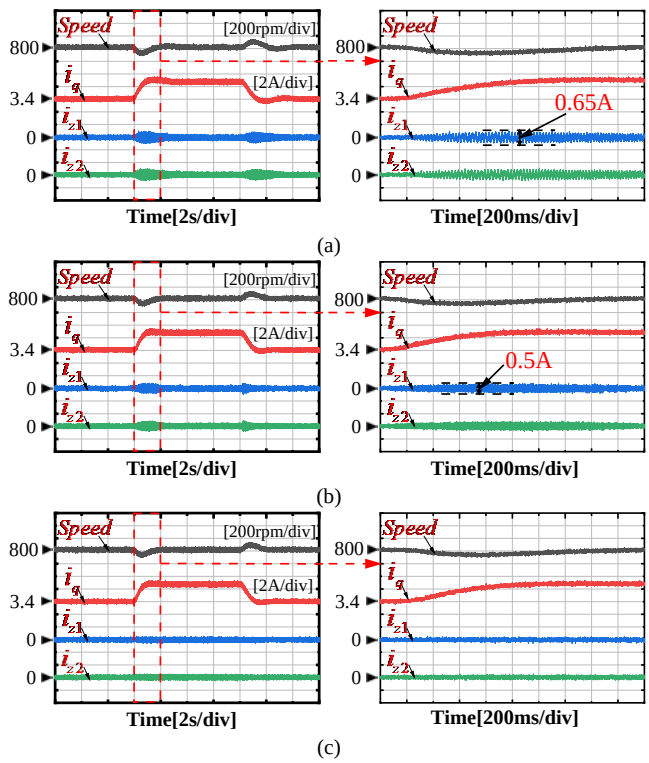

Fig. 14. Comparative experimental results of four different schemes with load variation. (a) Method 2. (b) Method 3. (c) Proposed method.

Fig. 14 shows the results of a load-variable experiment at 800 r/min, where the rated load is first applied and then removed. The results indicate that all methods exhibit slight speed fluctuations during the load transition. Due to the relatively slow loading process of the eddy current brake, the dynamic response time differences between the methods are not significant. However, these differences can be distinguished by observing the harmonic currents during the loading process. Figs. 14(a) and (b) show that, during the load transition, the harmonic currents i_{z1} and i_{z2} exhibit slight fluctuations, with amplitudes of 0.65 and 0.5 A, respectively. In contrast, the proposed method achieves superior harmonic current suppression, as i_{z1} and i_{z2} remain nearly constant throughout the load transition. This verifies that the proposed method can fully decouple the harmonic currents from the fundamental current. Therefore, the proposed method effectively responds to speed and load changes during dynamic operation, thereby enhancing system stability and improving dynamic response capability.

D. Code Execution Time

To assess whether the proposed method imposes a significant computational burden on the MCU, the code execution time of the five methods was measured under the same control cycle. The results are shown in Fig. 15. At a control frequency of 10 kHz (corresponding to a control cycle of 100 μs), the code execution times for the four methods were 18, 29, 27, and 32 μs, respectively. The results show that although the proposed method introduces the Goertzel algorithm, which incurs additional computational overhead and increases the processing load of the MCU to some extent, its execution time still accounts for only approximately one-third of the total control cycle, while maintaining real-time computing capabilities.

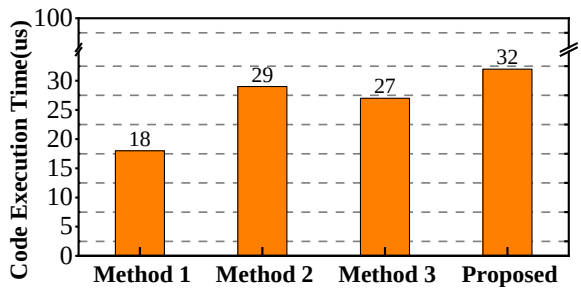

Fig. 15. Code execution time comparison.

E. Discussion

This paper proposes an LPF-free MSRF method, offering a new approach for harmonic current suppression. The method suppresses harmonic currents without the need for LPFs, thereby simplifying the system structure and enhancing stability. Specifically, the introduction of HTMCs effectively replaces the traditional LPF, avoiding issues such as delays and phase distortion introduced by filters. The Goertzel algorithm is employed to accurately capture signal fluctuations at specific target frequencies, allowing for harmonic amplitude extraction and HTMCs determination. Based on this strategy, the proposed method not only effectively suppresses harmonic currents but also prevents high-frequency harmonic interference without relying on filters.

Moreover, as described in Section III-A, the proposed HTMC is designed to reduce the amplitude of uncontrolled

harmonic currents. For the controlled 5th and 7th harmonics, HTMC acts merely as a coefficient, with minimal impact on the system. Compared to the methods in [28]-[29], the proposed method does not require harmonic subspace reconstruction, thus avoiding additional coordinate transformation processes. This approach demonstrates more stable harmonic current suppression and stronger dynamic performance during motor dynamic changes.

Additionally, the Goertzel algorithm updates the computed results recursively. Therefore, the HTMC obtained through the Goertzel algorithm can be periodically updated. This feature ensures that the method exhibits strong adaptability when responding to dynamic load and speed changes under complex operating conditions.

It is important to note that the updating of HTMC via the Goertzel algorithm and its application in the system are not sequential. If the Goertzel algorithm is still performing calculations, the HTMC will retain the value from the previous time step and will not wait for the Goertzel algorithm to complete. Thus, although the window-based Goertzel algorithm introduces some window delay, which results in a delayed HTMC update, it does not cause any delay in the system, nor does it affect the system's dynamic response. Experimental tests show that using fixed coefficients $k_5 = 0.5$ and $k_7 = 0.5$ satisfies all operational conditions. The introduction of the Goertzel algorithm enhances the flexibility of the control system, enabling adaptive adjustment and strengthening the adaptability of the proposed method.

However, the method also has some limitations. As shown in Fig. 6, the Goertzel-based approach can accurately extract harmonic amplitudes with minimal error in high-frequency scenarios. However, in low-frequency scenarios, the extraction error increases. To address this issue, we propose a piecewise method to determine the HTMC. When the harmonic current frequency is low, a fixed HTMC is used, while for sufficiently high harmonic frequencies, the Goertzel-based method is applied. This method ensures effective harmonic current suppression across the entire frequency range. Furthermore, as shown in Fig. 15, while the proposed method improves the system's dynamic performance, the window-based Goertzel algorithm increases the code execution time and consumes computational resources.

V. Conclusion

This paper has investigated harmonic current control for DTP-PMSM drives and proposed an LPF-free MSRF-based control method. The proposed approach addresses the performance degradation caused by filtering-based harmonic decoupling in conventional MSRF implementations, particularly under dynamic operating conditions where detection delay and phase distortion become significant. By introducing HTMCs, the filtering stage in the harmonic decoupling process is removed while independent regulation of multiple harmonic components is preserved within the MSRF framework. A Goertzel-based harmonic amplitude extraction scheme is employed to update the HTMCs in real time, enabling adaptive harmonic current control without harmonic plane reconstruction or additional coordinate transformations. Experimental validation confirms that the proposed low-pass-filter-free multi-synchronous rotating coordinate frame method effectively suppresses dominant harmonic currents and improves dynamic performance. Compared with other methods, the speed transition stabilization time is reduced by 19.3%, while the harmonic current suppression capability during load transients remains unaffected. Additionally, the method maintains feasible real-time computational complexity. Although the proposed method is validated on a DTP-PMSM system, the LPF-free MSRF formulation is applicable to MSRF-based multi-frequency current control problems where filter-induced delay limits dynamic performance. Further investigation will focus on evaluating its applicability under different operating conditions and system configurations.

Appendix

The transformation matrix for converting a neutral-point-isolated DTP-PMSM from the natural coordinate system to the stationary coordinate system based on the VSD method is as follows:

$$\boldsymbol{T}_{6s/2s} = \frac{1}{6}\begin{bmatrix} 2 & -1 & -1 & \sqrt{3} & -\sqrt{3} & 0 \\ 0 & \sqrt{3} & -\sqrt{3} & 1 & 1 & -2 \\ 2 & -1 & -1 & -\sqrt{3} & \sqrt{3} & 0 \\ 0 & -\sqrt{3} & \sqrt{3} & 1 & 1 & -2 \end{bmatrix} \tag{A1}$$

The transformation matrix for converting a neutral-point isolated DTP-PMSM from the natural coordinate system to the stationary coordinate system based on the double αβ-method is as follows:

$$\boldsymbol{T}_{6s/2\alpha\beta} = \frac{1}{3}\begin{bmatrix} 2 & -1 & -1 & 0 & 0 & 0 \\ 0 & \sqrt{3} & -\sqrt{3} & 0 & 0 & 0 \\ 0 & 0 & 0 & \sqrt{3} & -\sqrt{3} & 0 \\ 0 & 0 & 0 & 1 & 1 & -2 \end{bmatrix} \tag{A2}$$

References

[1] L. X. Tang, and G. J. Su, "High-performance Control of Two Three-phase Permanent-magnet Synchronous Machines in an Integrated Drive for Automotive Applications," *IEEE Trans. on Power Electron.*, vol. 23, no. 6, pp. 3047–3055, Nov. 2008.

[2] L. S. Huang, J. H. Ji, and W. X. Zhao *et al.*, "Direct Torque Control for Dual Three-phase Permanent Magnet Motor with Improved Torque and Flux," *IEEE Trans. on Energy Convers.*, vol. 37, no. 4, pp. 2385–2397, Dec. 2022.

[3] Y. Ren, and Z. Q. Zhu, "Enhancement of Steady-state Performance in Direct-torque-controlled Dual Three-phase Permanent-magnet Synchronous Machine Drives with Modified Switching Table," *IEEE Trans. on Ind. Electron.*, vol. 62, no. 6, pp. 3338–3350, Jun. 2015.

[4] M. R. Gu, Z. Wang, and B. Wang, "Optimization of Torque Ripple for Low-carrier-ratio Dual Three-phase PMSM with Pulse Pattern Control," *IEEE Trans. on Power Electron.*, vol. 38, no. 12, pp. 15091–15096, Dec. 2023.

[5] Z. F. Song, F. Y. Mao, and Y. J. Cui *et al.*, "An Fault-tolerant Control

Strategy based on Decoupling between Reference Tracking and Periodic Disturbance Attenuation for Dual-three-phase Permanent Magnet Synchronous Machine," *Transactions of China Electrotechnical Society*, vol. 38, no. 2, pp. 435–450, Jan. 2023.

[6] K. Zhang, M. D. Fan, and Y. Yang *et al*., "An Improved Adaptive Selected Harmonic Elimination Algorithm for Current Measurement Error Correction of PMSMs," *IEEE Trans. on Power Electron*., vol. 36, no. 11, pp. 13128–13138, Nov. 2021.

[7] G. D. Feng, C. Y. Lai, and W. L. Li *et al*., "Dual Reference Frame based Current Harmonic Minimization for Dual Three-phase PMSM Considering Inverter Voltage Limit," *IEEE Trans. on Power Electron*., vol. 36, no. 7, pp. 8055–8066, Jul. 2021.

[8] D. Yazdani, S. Ali Khajehoddin, and A. Bakhshai *et al*., "Full Utilization of the Inverter in Split-phase Drives by Means of a Dual Three-phase Space Vector Classification Algorithm," *IEEE Trans. on Ind. Electron.*, vol. 56, no. 1, pp. 120–129, Jan. 2009.

[9] K. Marouani, L. Baghli, and D. Hadiouche *et al*., "A New PWM Strategy based on a 24-sector Vector Space Decomposition for a Six-phase VSI-fed Dual Stator Induction Motor," *IEEE Trans. on Ind. Electron.*, vol. 55, no. 5, pp. 1910–1920, May 2008.

[10] K. Wang, Z. Q. Zhu, and Y. Ren *et al*., "Torque Improvement of Dual Three-phase Permanent-magnet Machine with Third-harmonic Current Injection," *IEEE Trans. on Ind. Electron.*, vol. 62, no. 11, pp. 6833–6844, Nov. 2015.

[11] Y. S. Hu, Z. Q. Zhu, and M. Odavic, "Torque Capability Enhancement of Dual Three-phase PMSM Drive with Fifth and Seventh Current Harmonics Injection," *IEEE Trans. on Ind. Appl*., vol. 53, no. 5, pp. 4526–4535, Sept.-Oct. 2017.

[12] G. D. Feng, C. Y. Lai, and M. Kelly *et al*., "Dual Three-phase PMSM Torque Modeling and Maximum Torque Per Peak Current Control Through Optimized Harmonic Current Injection," *IEEE Trans. on Ind. Electron.*, vol. 66, no. 5, pp. 3356–3368, May 2019.

[13] Y. S. Hu, Z. Q. Zhu, and K. Liu, "Current Control for Dual Three-phase Permanent Magnet Synchronous Motors Accounting for Current Unbalance and Harmonics," *IEEE Journal of Emerg. and Sel. Topics in Power Electron.*, vol. 2, no. 2, pp. 272–284, Jun. 2014.

[14] X. Chen, Z. R. Zhang, and L. Yu *et al*., "Current Harmonic Suppression Method of Doubly Salient Electro-magnetic Machine based on Improved Quasi Proportional Resonant Control," *Transactions of China Electrotechnical Society*, vol. 38, no. 14, pp. 3836–3848+3861, Jul. 2023.

[15] Y. G. Li, Y. S. Hu, and Z. Q. Zhu, "Current Harmonics and Unbalance Suppression of Dual Three-phase PMSM based on Adaptive Linear Neuron Controller," *IEEE Trans. on Energy Convers.*, vol. 38, no. 4, pp. 2353–2363, Dec. 2023.

[16] Y. X. Xu, B. Y. Zheng, and G. Wang *et al*., "Current Harmonic Suppression in Dual Three-phase Permanent Magnet Synchronous Machine with Extended State Observer," *IEEE Trans. on Power Electron.*, vol. 35, no. 11, pp. 12166–12180, Nov. 2020.

[17] G. X. Lu, J. Y. Su, and G. J. Yang *et al*., "Transitional Period Harmonic Current Analysis and Suppression in Dual Three-phase PMSMs Using Generalized Integrators," *IEEE Journal of Emerg. and Sel. Topics in Power Electron.*, vol. 12, no. 4, pp. 3862–3874, Aug. 2024.

[18] L. C. Yan, Z. Q. Zhu, and J. Qi *et al*., "Multiple Synchronous Reference Frame Current Harmonic Regulation of Dual Three Phase PMSM with Enhanced Dynamic Performance and System Stability," *IEEE Trans. on Ind. Electron.*, vol. 69, no. 9, pp. 8825–8838, Sept. 2022.

[19] Y. R. Miao, P. Y. Song, and M. S. Lv *et al*., "Design of Cost Function without Weighting Factor for Predictive Torque Control of Surface-mounted Permanent Magnet Synchronous Motor," *Transactions of China Electrotechnical Society*, vol. 38, no. 12, pp. 3141–3150, Jun. 2023.

[20] Z. Y. Lan, J. Luo, and Y. H. Li *et al*., "Model Prediction Torque Control for Permanent Magnet Synchronous Motor based on the Fast Selection Table," *Transactions of China Electrotechnical Society*, vol. 38, no. 21, pp. 5749–5757, Nov. 2023.

[21] W. S. Wang, C. H. Liu, and Z. X. Song *et al*., "Harmonic Current Suppression for Dual Three-phase PMSM based on Deadbeat Control and Disturbance Observer," *IEEE Trans. on Ind. Electron.*, vol. 70, no. 4, pp. 3482–3492, Apr. 2023.

[22] L. S. Huang, J. H. Ji, and W. X. Zhao *et al*., "Duty-ratio-based Direct Torque Control with Enhanced Harmonic Current Suppression for Dual-three-phase Permanent Magnet Motor," *IEEE Trans. on Power Electron*., vol. 37, no. 9, pp. 11098–11108, Sept. 2022.

[23] Y. Ren, and Z. Q. Zhu, "Reduction of Both Harmonic Current and Torque Ripple for Dual Three-phase Permanent-magnet Synchronous Machine Using Modified Switching-table-based Direct Torque Control," *IEEE Trans. on Ind. Electron.*, vol. 62, no. 11, pp. 6671–6683, Nov. 2015.

[24] G. Liang, S. Huang, and W. Liao *et al*., "An Optimized Modulation of Torque and Current Harmonics Suppression for Dual Three-phase PMSM," *IEEE Trans. on Transport. Electrific*., vol. 10, no. 2, pp. 3443–3454, Jun. 2024.

[25] B. Y. Zheng, J. B. Zou, and Y. X. Xu *et al*., "High-frequency Current Harmonic Analysis and Suppression in Dual Three-phase PMSMs with Advanced Carrier Phase-shift PWM," *IEEE Trans. on Power Electron*., vol. 39, no. 2, pp. 2569–2581, Feb. 2024.

[26] P. L. Chapman, and S. D. Sudhoff, "A Multiple Reference Frame Synchronous Estimator/regulator," *IEEE Trans. on Energy Convers*., vol. 15, no. 2, pp. 197–202, Jun. 2000.

[27] G. D. Feng, C. Y. Lai, and J. B. Tian *et al*., "Multiple Reference Frame based Torque Ripple Minimization for PMSM Drive Under Both Steady-state and Transient Conditions," *IEEE Trans. on Power Electron*., vol. 34, no. 7, pp. 6685–6696, Jul. 2019.

[28] L. C. Yan, Z. Q. Zhu, and J. Qi *et al*., "Suppression of Major Current Harmonics for Dual Three-phase PMSMs by Virtual Multi Three-phase Systems," *IEEE Trans. on Ind. Electron.*, vol. 69, no. 6, pp. 5478–5490, Jun. 2022.

[29] X. C. Ma, B. Li, and G. D. Li *et al*., "Natural Decoupling and Regulation of Harmonic Currents in Dual Three-phase Permanent Magnet Synchronous Machine," *IEEE Journal of Emerg. and Sel. Topics in Power Electron.*, vol. 14, no. 1, pp. 1097–1111, Feb. 2026.

[30] T. F. Qiu, X. H. Wen, and F. Zhao, "Adaptive-linear-neuron-based Dead-time Effects Compensation Scheme for PMSM Drives," *IEEE Trans. on Power Electron*., vol. 31, no. 3, pp. 2530–2538, Mar. 2016.

Yulei Yang received the B.E. and M.E. degrees in electrical engineering from Harbin Institute of Technology, Harbin, China, in 2019 and 2021, respectively, and is currently pursuing the Ph.D. degree in electrical engineering at the same university.

His research interests focus on motor drives and harmonic current suppression.

Qian Wang (Member, IEEE) was born in Henan, China, in 1982. He received the Ph.D. degree in electrical engineering from Harbin Institute of Technology, Harbin, China, in 2010.

He is currently a Professor with the Department of Electrical Engineering, Harbin Institute of Technology, Harbin, China. His research interest covers novel permanent magnet motors, linear machines, and permanent magnet flexible transmission.

Fangrui Wei received the B.Eng. and M.Sc. degrees in electrical engineering from Harbin Institute of Technology, Harbin, China, in 2016 and 2018, respectively, and Ph.D. degree in the University of Sheffield, Sheffield, UK. He is currently working as lecture in Harbin Institute of Technology, Harbin, China.

His current research interests include design and analysis of permanent magnet machines and thermal management in electric machine.

Yichen Yu received the B.E. degree in electrical engineering from Harbin Institute of Technology, Harbin, China, in 2022, where he is currently pursuing the Ph.D. degree in electrical engineering.

His research interests include magnetic screw and linear actuators.